J. Fluid Mech. (2024), *vol*. 999, A63, doi:10.1017/jfm.2024.948

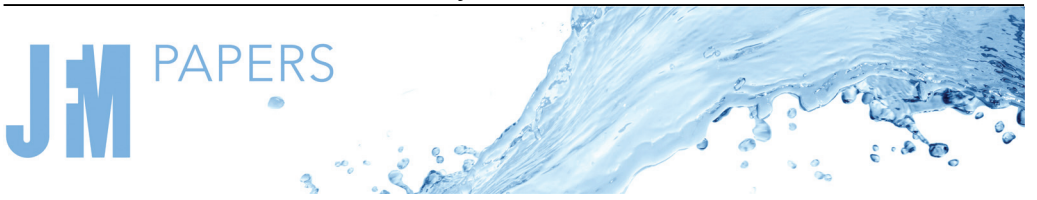

Friction drag reduction of Taylor–Couette flow over air-filled microgrooves

Xiaochao Liu[1], Chenxi You[1], Yanlin Cao[1], Baorui Xu[1], Yantao Yang[1,2], Hongyuan Li[1,2,3], Pengyu Lv[1,2], Chao Sun[4,5] and Huiling Duan[1,3,†]

[1]State Key Laboratory for Turbulence and Complex Systems, Department of Mechanics and Engineering Science, College of Engineering, Peking University, Beijing 100871, PR China

[2]Laoshan Laboratory, Qingdao 266237, PR China

[3]CAPT, HEDPS and IFSA Collaborative Innovation Center of MoE, Peking University, Beijing 100871, PR China

[4]Department of Engineering Mechanics, School of Aerospace Engineering, Tsinghua University, Beijing 100084, PR China

[5]New Cornerstone Science Laboratory, Center for Combustion Energy, Department of Energy and Power Engineering, Tsinghua University, Beijing 100084, PR China

(Received 22 May 2024; revised 10 August 2024; accepted 20 September 2024)

Reducing drag under high turbulence is a critical but challenging issue that has engendered great concern. This study utilizes hydrophilic tips in superhydrophobic (SHP) grooves to enhance the stability of plastron, which results in a considerable drag reduction (DR) up to 62 %, at Reynolds number (Re) reaching 2.79×10^4. The effect of the spacing width w of the microgrooves on both DR and flow structures is investigated. Experimental results demonstrate that DR increases as either microgroove spacing w or Re increases. The velocity fields obtained using particle image velocimetry indicate that the air-filled SHP grooves induce a considerable wall slip. This slip significantly weakens the intensity of Taylor rolls, reduces local momentum transport, and consequently lowers drag. This phenomenon becomes more pronounced with increasing w. Furthermore, to quantify the multiscale relationship between global response and geometrical as well as driving parameters, $DR \sim (w, \phi_s, Re)$, a theoretical model is established based on angular momentum defect theory and magnitude estimate. It is demonstrated that a decrease in the surface solid fraction can reduce wall shear, and an increase in the groove width can weaken turbulence kinetic energy production, rendering enhanced slip and drag reduction. This research has implications for designing and optimizing turbulent-drag-reducing surfaces in various engineering applications, such as transportation and marine engineering.

Key words: drag reduction, turbulence control, Taylor–Couette flow

† Email address for correspondence: hlduan@pku.edu.cn

1. Introduction

Frictional drag reduction is of great significance in many engineering applications. Extensive research has been conducted on superhydrophobic (SHP) surfaces, because microstructures can capture air pockets underwater, creating a liquid–gas interface that functions as a slip boundary, leading to reduced drag in turbulent flows (Rothstein 2010). Numerical simulations and experimental studies have been carried out to investigate drag reduction (*DR*) of turbulent flow on SHP surfaces. The numerical results suggested consistently that SHP surfaces can achieve significant *DR* in turbulence (Min & Kim 2004; Fukagata, Kasagi & Koumoutsakos 2006; Martell, Rothstein & Perot 2010; Park, Park & Kim 2013; Rastegari & Akhavan 2015; Jung, Choi & Kim 2016; Im & Lee 2017). Conversely, experimental results did not converge to any clear trend. Some studies reported that increasing the size and spacing of microstructures on SHP surfaces could result in greater *DR* (Daniello, Waterhouse & Rothstein 2009; Park, Sun & Kim 2014), while others showed little *DR* or even drag increase when microstructure size increases (Gose *et al.* 2018). Notably, in turbulent Taylor–Couette (TC) flow, by using V-shaped grooves, Rosenberg *et al.* (2016) demonstrated that varying Reynolds number (*Re*) has no significant impact on *DR*. In contrast, Van Buren & Smits (2017) obtained a maximum *DR* of about 45 % in turbulent TC flow by varying *Re* as well as the width of longitudinal rectangular grooves. Both Rosenberg *et al.* (2016) and Van Buren & Smits (2017) noted that disruption of the plastron was observed during the experiment. Park, Choi & Kim (2021) pointed out that the deterioration or depletion of the plastron is a significant reason for the inconsistency of *DR* mechanisms in turbulent flows. The aforementioned studies indicate that further exploration is warranted regarding the effect of microstructure sizes on *DR*, particularly in cases involving stable air plastron.

The magnitude of *DR* depends not only on the geometry and size of the microstructure, but also on the *Re* value of the base flow. Both direct numerical simulations and experiments suggest that the magnitude of *DR* decreases with increasing *Re* on the microstructure surface with a given geometry and size (in wall units) (Rastegari & Akhavan 2018, 2019). In contrast, other experimental studies have reported an enhancement of *DR* with increasing *Re* in turbulent boundary layer flows (Zhang *et al.* 2015) or in turbulent TC flows (Srinivasan *et al.* 2015; Rosenberg *et al.* 2016; Van Buren & Smits 2017). Srinivasan *et al.* (2015) tested SHP surfaces with random roughness in TC flows and observed that the magnitude of *DR* increased with increasing *Re*, achieving approximately 22 % at the highest *Re* value tested. They derived a correlation between the dimensionless effective slip length ($b^+ = b/\delta_\nu$) and the friction coefficient as well as *Re*, without focusing on the structural parameters. There is a complex multiscale interaction between the microstructural parameters and the flow parameter (*Re*) on the magnitude of *DR*, which needs to be explored further.

In turbulent flows, the drag reduction mechanism of SHP microstructures is usually attributed to the effective slip at the solid wall, which significantly influences the near-wall turbulence structures (Park *et al.* 2021). Research showed that the streamwise slip induced by microstructures in turbulent channel flow can inhibit near-wall turbulence structures by modifying the spanwise sweep and ejection dynamics of vortices (Park *et al.* 2013; Jelly, Jung & Zaki 2014). Conversely, spanwise slip has the potential to amplify streamwise turbulence structures and may even cause an overall increase in drag (Min & Kim 2004; Fukagata *et al.* 2006). Furthermore, investigations by Im & Lee (2017) have explored the impact of alternating no-slip and slip boundary conditions on flow structures in turbulent pipe and channel flow, and found that increased spanwise slip can enhance secondary vortex structures, resulting in a higher *DR*. Recent numerical and experimental studies

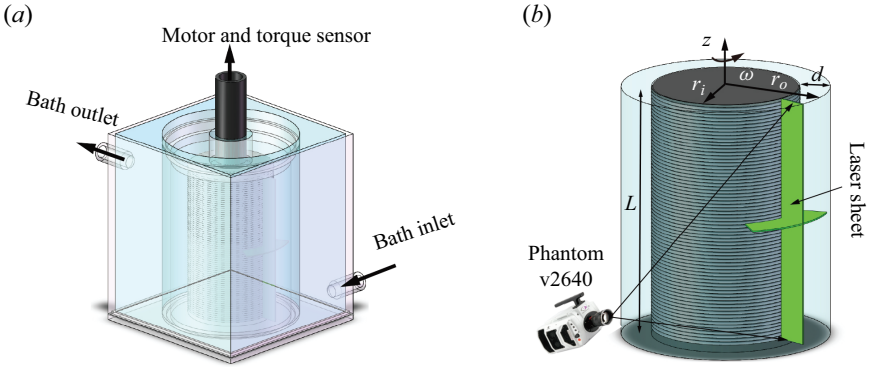

Figure 1. The experimental set-up. (*a*) Sketch of the experimental set-up including the TC facility. (*b*) PIV measurements in the r–θ plane and r–z plane.

by Jeganathan, Alba & Ostilla-Mónico (2021) and Jeganathan *et al.* (2023) have also investigated the effects of alternative slip and no-slip boundary conditions on secondary flow and torque in turbulent TC flow, showing that the SHP treatment with appropriate axial spacing can effectively reduce the impact of vortices. While microstructural features and Re significantly impact the effective slip (Srinivasan *et al.* 2015; Rajappan *et al.* 2019; Li *et al.* 2020*a*,*b*; Ji *et al.* 2023), the comprehensive analysis of the influence of variations in air-filled groove width and Re on the slip boundary, thus affecting secondary flow and modulating DR in turbulent shear flow, is lacking and warrants further exploration.

This study explores experimentally the effects of spacing width w and Re on DR, and elucidates the underlying mechanisms. A theoretical model is also developed to describe the multiscale relationship between global response and geometrical and driving parameters.

2. Experimental facility

The TC facility is illustrated in figure 1(*a*). The inner cylinder with V-shaped microgrooves was manufactured using computer numerical control technology with precision approximately 20 μm and was mounted on the freely rotating spindle of the rheometer (DHR-2, TA Instruments, USA). The radii of the inner and outer cylinders are $r_i = 25 \pm 0.02$ mm and $r_o = 35 \pm 0.02$ mm, respectively, with the gap between the two cylinders $d = r_o - r_i = 10$ mm, corresponding to a radius ratio $\eta = r_i/r_o = 0.714$. The height of the set-up is $L = 84 \pm 0.02$ mm, with aspect ratio $\Gamma = L/d = 8.4$. Throughout the experiments, ultra-pure water was used as the working liquid, maintained at a constant temperature with precision ±0.5 K, which was achieved by a quartz glass cubic circulating bath surrounding the TC system (see figure 1*a*).

To capture velocity in the r–θ plane at mid-height $L/2$ and the r–z plane, high-resolution particle image velocimetry (PIV) was employed. Fluorescent polymer tracer particles (Dantec FPP-RhB-10 1–20 μm) were added to the working fluid, and a laser sheet of thickness approximately 0.5 mm illuminated the tracer particles (see figure 1*b*). The camera lens was equipped with an Edmund High-Performance Long-pass 550 nm filter (910072, Beiting Measurement Technique, China) to optimize particle contrast. The velocity fields were captured with a high-resolution camera (Phantom v2640, USA) with 2048 × 1952 pixels. The PIV images were post-processed in MATLAB's open-source PIVlab software (Thielicke & Sonntag 2021) using multi-step interrogation windows

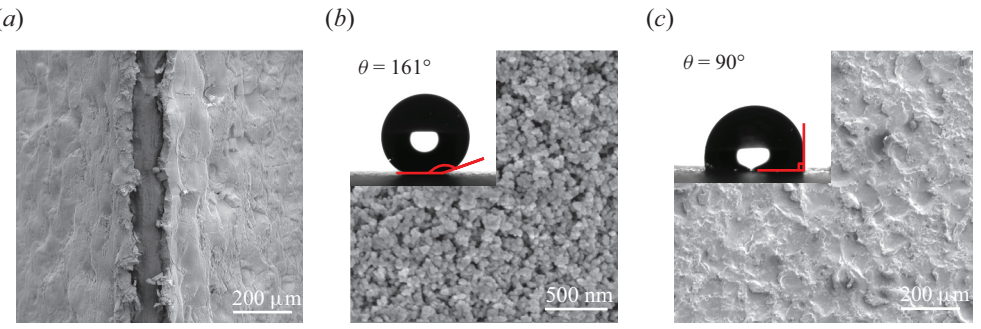

Figure 2. Scanning electron microscopy of structured surfaces: (*a*) V-groove tips with hydrophilic treatment; (*b*) SHP surface; (*c*) hydrophilic-treated surface. The insets show the contact angle of a 5 μL ultra-pure water droplet over the corresponding surfaces.

ranging from 64 × 64 to 16 × 16 pixels. These fields were initially calculated in Cartesian coordinates and subsequently converted into polar coordinates.

To analyse the groove-induced *DR* effects, we fabricated the grooves with the shape of isosceles triangles and widths $w = 600, 800, 1000, 1200$ μm (dimensionless form $\tilde{w} = w/d$) on the inner rotor. A layer of styrene ethylenebutylenestyrene copolymer chemical coating was applied, and subsequently SHP nanoparticles were sprayed (Cao *et al.* 2024). Moreover, a hydrophilic treatment was performed on the tips of the V-grooves. The basic idea of hydrophilic treatment on the tips of grooves is to remove the SHP coating by direct polishing so that the hydrophilic substrate will be exposed, which involves two main steps. (i) We fabricate a hollow cylinder made of resin by three-dimensional printing. The inner surface of the hollow cylinder precisely matches the tips of grooves on the inner rotor. (ii) By the three-dimensional printed hollow cylinder covering and sliding on the inner rotor, the SHP coating on the tips of grooves is polished, thus the hydrophilic substrate underneath the SHP coating is exposed. Figure 2(*a*) displays a scanning electron micrograph of a hydrophilic-treated V-shaped groove, where the exposed groove tip can be observed.

To characterize the contact angle, tests have been conducted on flat surfaces. Figure 2(*b*) shows a scanning electron micrograph of the SHP surface with contact angle 161°. We destroyed the SHP coating on the flat surface by using the same hydrophilic treatment to expose the hydrophilic substrate, on which the contact angle was reduced to 90°, as shown in figure 2(*c*). The hydrophilic treatment significantly alters the energy states of the SHP surface, particularly at the tips of the grooves. This alteration generates an energy barrier, restricts the movement of air, and strengthens the stability of the liquid–gas interface (see figures 3*a*,*b*). The width of each hydrophilic tip (l_{tip}) was measured to be 100 μm using confocal microscopy (see figure 3*c*).

Hydrophilic tips of V-grooves play an important role in pinning and stabilizing the liquid–gas interface, especially under highly turbulent flow. Experimental results showed that the liquid–gas interfaces in V-grooves with hydrophilic tips underwent two distinct states as the rotating speed increased, as shown in figure 3(*b*). Taking the microgroove width 1200 μm as an example, in the range $\omega_i < 40$ rad s^{-1}, the liquid–gas interface remained stationary and stable; in the range $40 < \omega_i < 100$ rad s^{-1}, the interface fluctuated but stayed pinned to the V-grooves. In contrast, the plastron in V-grooves without hydrophilic tips rises due to the buoyancy and pressure, resulting in uneven air

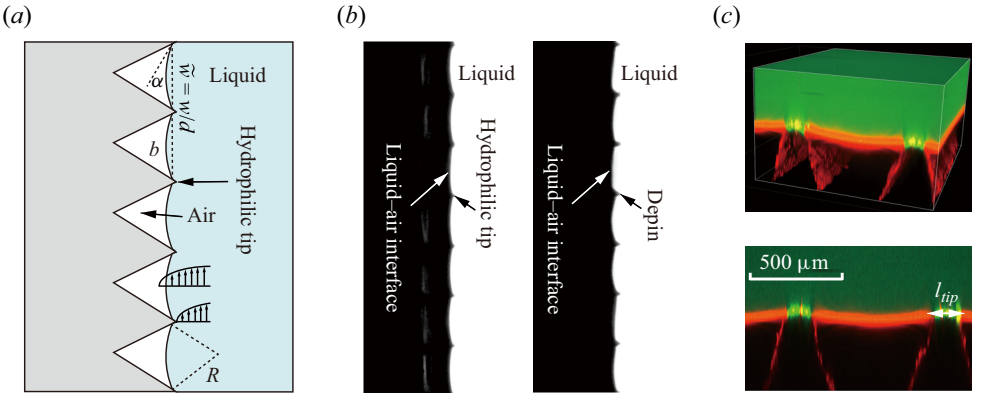

Figure 3. (*a*) V-shaped grooves in TC flow featuring a hydrophilic tip. (*b*) Two states of the liquid–gas interface in the V-groove with hydrophilic tips, at $Re = 1.12 \times 10^4$ (on the left) and $Re = 4.21 \times 10^4$ (on the right). At $Re = 4.21 \times 10^4$, the liquid–gas interface is depinned from the tips.(*c*) Confocal microscopy images of the hydrophilic tips of air-filled grooves.

distribution (see the supplementary movie available at https://doi.org/10.1017/jfm.2024.948). The experimental evidence for a robust air plastron is presented in Appendix B.

The torque of the inner rotor was measured using contactless sensors located in the rheometer head, while the outer cylinder remained stationary. For pure inner rotation, Re is defined with the gap width d and the velocity of the inner cylinder $V_i = r_i\omega_i$ as

$$Re = \frac{r_i\omega_i d}{\nu}, \tag{2.1}$$

where ω_i is the angular velocity of the inner cylinder, and ν is the kinematic viscosity. In the present work, ω_i ranged from 10 to 100 rad s^{-1}, resulting in Re ranging from 2.7×10^3 to 2.79×10^4. The total torque of the TC system (T_{total}) was comprised of the torque exerted by the side wall of the inner rotor T and the torque induced by the von Kármán flow at the end plates (T_{end}) (Greidanus, Delfos & Westerweel 2011; Hu *et al.* 2017; Wang *et al.* 2022; Xu *et al.* 2023), and the isolation of T from T_{total} is detailed in Appendix A. For each experiment, the torque measurements were repeated five times, and the averaged value of T was used, with the standard deviations below 2 %.

3. Results and discussion

3.1. *Drag reduction*

In this subsection, we experimentally examine the effects of varying microstructure size and driving strength on the global torque. The dimensionless wall shear stress is typically expressed using the skin friction coefficient, which is calculated from torque versus rotational speed data using the expressions

$$C_f = \frac{2\tau_i}{\rho V_i^2} = 2\left(\frac{u_\tau}{V_i}\right)^2, \tag{3.1}$$

where $\tau_i = T/(2\pi r_i^2 L)$ is average inner wall shear stress, and $u_\tau = (\tau_i/\rho)^{1/2}$ is the friction velocity. Furthermore, the microstructure dimensions and driving strength can be characterized by the width of grooves $\tilde{w}$ and Re based on the inner cylinder,

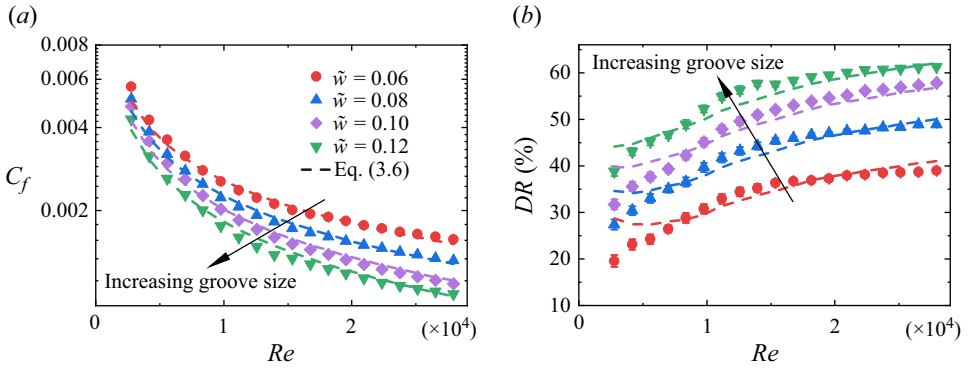

Figure 4. (*a*) Plot of C_f as a function of *Re*, with various SHP groove widths $\tilde{w}$. (*b*) Drag reduction plotted against *Re*. In the plots, the predictions of the theoretical model (dashed lines) are very close to the experimental data (solid symbols), which proves that the theoretical model is highly accurate in predicting C_f and *DR* for different groove widths.

respectively. The magnitude of drag reduction is denoted as *DR* and calculated as $DR = 1 - C_{f,w}/C_{f,smooth}$.

The impacts of varying *Re* at different groove widths $\tilde{w}$ on the dimensionless wall shear stress C_f are illustrated in figure 4(*a*), and the *DR* in figure 4(*b*). Specifically, as the groove widens, the dimensionless wall shear stress C_f declines, leading to a larger *DR*. Notably, a significant drag reduction has been observed in our experimental set-up, reaching 62 % at groove width $\tilde{w} = 0.12$ and $Re = 2.79 \times 10^4$. Moreover, figure 4(*b*) exhibits an uninterrupted increase of *DR*, in contrast to the existence of the decreasing trend observed in previous experimental studies (Rosenberg *et al.* 2016; Van Buren & Smits 2017). The continuous growth of *DR* indicates a more robust air layer captured in grooves over a wider range of *Re* and *w* in our research. Actually, the sustainable *DR* at high *Re*, up to $Re = 2.79 \times 10^4$, can be attributed to the hydrophilic treatment at the groove tips (see supplementary movie) to achieve a stable presence of the air layer.

3.2. *Angular momentum transport*

To gain a deeper understanding of the drag reduction mechanism of air-filled grooves in TC flow, the angular velocity and flow organization are investigated with high-resolution PIV and the measurement methodology shown in figure 1(*b*). The angular velocity is measured at mid-height at $Re = 1.12 \times 10^4$ for each value of $\tilde{w}$. In TC flows, the angular velocity ω, rather than the azimuthal velocity u_θ, demonstrates the intrinsic property of transportation and exhibits an appropriate log law (Grossmann, Lohse & Sun 2016), with the slope λ^{-1} of the shear- and curvature-affected logarithmic region, as shown in figure 5(*a*). Here, the superscript '+' denotes non-dimensionalization in terms of inner wall units, i.e. $y^+ = (r - r_i)/\delta_\nu$ and $\omega^+ = (\omega_i - \omega)/(u_\tau/r_i)$, with u_τ and $\delta_\nu = \nu/u_\tau$. In figure 5(*b*), the profiles of diagnostic function $y^+ \,\mathrm{d}\omega^+/\mathrm{d}y^+$ not only collapse but also plateau at $1/\lambda \approx 1/0.64$, consistent with the results of Berghout *et al.* (2020, 2021). Here, the Obukhov length $L_c = u_\tau/\kappa(\omega_i + \Delta\omega)$ is introduced to rescale the wall-normal distance to incorporate the curvature effect. Notably, as $\tilde{w}$ increases, the ω^+ profiles shift upwards by $\Delta\omega^+$ (see figure 5*a*), indicating a reduction in drag and the presence of a finite slip length at the inner boundary, where the shift $\Delta\omega^+$ is calculated by the intercept

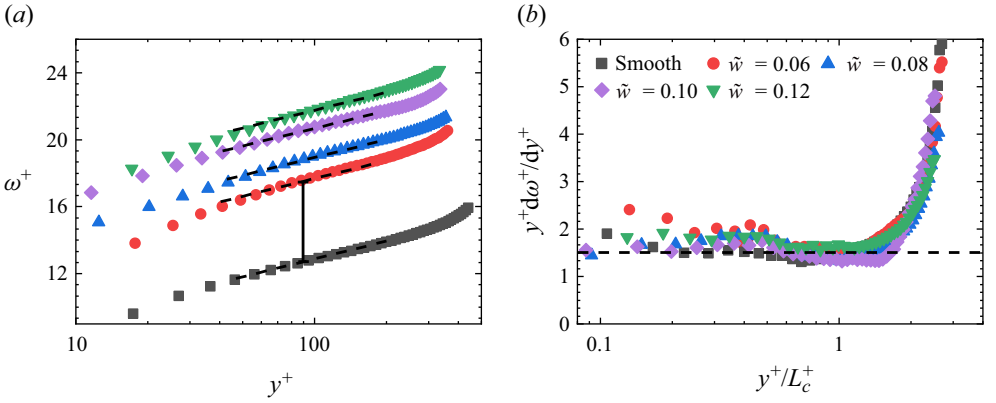

Figure 5. Angular velocity profiles based on the experiments with $\omega_i = 40$ rad s^{-1}. (*a*) Mean angular velocity ω^+ as a function of y^+ for varying $\tilde{w}$. (*b*) Diagnostic function $y^+ \mathrm{d}\omega^+/\mathrm{d}y^+$, with wall-normal distance rescaled by Obukhov length L_c.

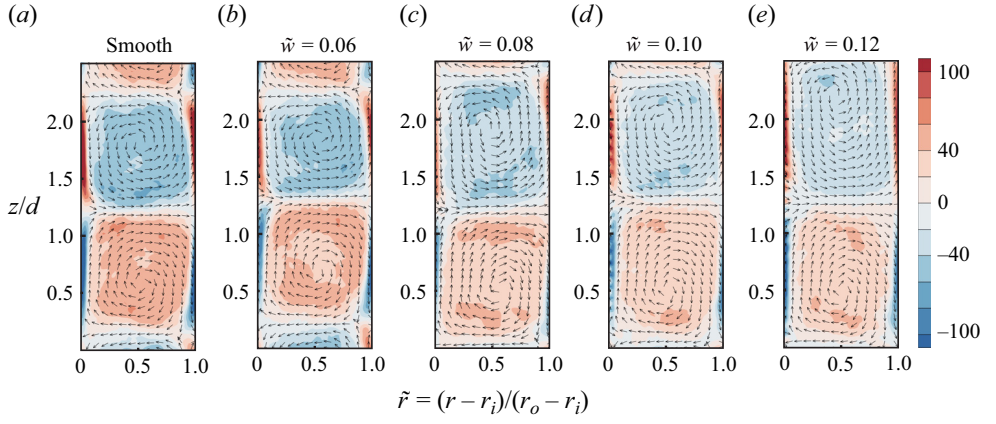

Figure 6. Radial–axial vorticity fields in the gap measured at $Re = 1.12 \times 10^4$. The axial position is normalized by the annular gap width.

difference between the mean angular velocity profile $\omega^+(y^+)$ in the logarithmic region of the grooved surfaces and that of the smooth wall.

The slip boundary achieved by the grooved SHP surface can considerably reduce the angular velocity gradient $\partial_r \langle\omega\rangle_{A,t}$ near the wall, and thus give rise to lower shear stress. The slip boundary affects the flow in the bulk region because of the conservation of the angular velocity current along the radius (Eckhardt, Grossmann & Lohse 2007; Zhu *et al.* 2016). This effect manifests in the bulk region through changes in the characteristics of Taylor rolls, including their intensity and distribution. Taylor rolls, one of the typical secondary flows in a TC system, play a crucial role in the convective part of the angular velocity current along the radius (Brauckmann & Eckhardt 2013; Ostilla-Mónico *et al.* 2016). Figure 6 shows the distribution of the axisymmetric azimuthal vorticity $\omega_\theta = \partial u_r/\partial z - \partial u_z/\partial r$, and velocity vectors for air-filled grooves of varying $\tilde{w}$ in TC flow at $Re = 1.12 \times 10^4$, plotted in the r–z plane. The intensity of the Taylor rolls for the smooth inner rotor is stronger than that of the air-filled grooves rotor, and their axial position varies slightly with $\tilde{w}$.

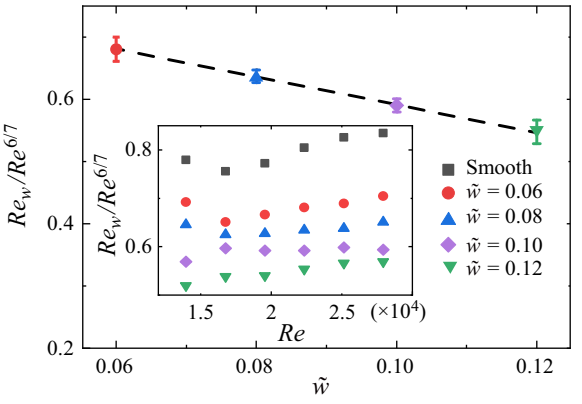

Figure 7. Wind Reynolds number Re_w compensated by $Re^{6/7}$ as a function of $\tilde{w}$, with the inset showing the original data of Re_w varying with Re at different $\tilde{w}$.

The strength of Taylor rolls can be represented quantitatively by the wind Reynolds number, denoted as $Re_w = \sigma(\langle u_r \rangle_t)\, d/\nu$, where $\sigma(\langle u_r \rangle_t)$ is the spatial standard deviation of the time-averaged radial velocity field $\langle u_r \rangle_t$ in the r–z plane. Moreover, $\langle u_r \rangle_t$ values obtained in experiments at $Re = 1.12 \times 10^4$ are presented in Appendix C. The experimental results of Re_w as a function of Re at different $\tilde{w}$ are depicted in the inset of figure 7, which substantiates the theoretical proposition that $Re_w \propto Re^{6/7}$ (Grossmann & Lohse 2011; van der Veen *et al.* 2016). Meanwhile, figure 7 demonstrates that Re_w of the air-filled grooves is lower than that of the smooth surface. Increasing the width of the grooves can further decrease Re_w, indicating a decrease in the intensity of the secondary flow. This reduction in secondary flow intensity consequently reduces the radial angular momentum transport, thereby increasing DR.

To sum up, the substantial and sustainable DR in § 3.1 corresponds to declined angular momentum transport and modified flow organizations, and can be attributed primarily to the considerable and stable slip length generated by the air-filled V-grooved surface featuring a hydrophilic tip.

3.3. *Theoretical model*

It has been suggested that drag reduction with air-filled microstructure surfaces depends not only on the geometrical parameters of the microstructure but also on the driving strength of the system (see figure 4), i.e.

$$DR = DR(w, \phi_s, Re). \tag{3.2}$$

As suggested by Park *et al.* (2014), we scale the groove width with the viscous length scale of the flow such that $w^+ = w\nu^{-1}\sqrt{\tau_i/\rho}$. In this subsection, an analytical expression of this relationship is presented based on angular momentum defect theory and magnitude estimate.

The derivation of (3.2) involves two steps due to the inherent multi-dimensionality of this problem. First, Srinivasan *et al.* (2015) proposed a modified skin friction law in turbulent TC flows ($Re > Re_c \approx 14\,000$) which accounts for wall slip:

$$\sqrt{\frac{2}{C_f}} = M \ln\left(Re\sqrt{\frac{C_f}{2}}\right) + N + b^+, \tag{3.3}$$

where $b^+ = b/\delta_v = [b/(r_o - r_i)]\, Re\sqrt{C_f/2}$ represents the dimensionless effective slip length, the geometry-dependent constants $M = 5.43$ and $N = -9.59$ are determined based on the no-slip case in our experimental set-up, and C_f is the skin friction coefficient.

Equation (3.3) illustrates the correlation between macroscopic variables, namely $DR = DR(b^+, Re)$ or $C_f = C_f(b^+, Re)$. Next, efforts have been made to bridge the gap between small-scale surface features and large-scale flow response. The latter is characterized primarily by the dimensionless slip length $b^+ = b^+(w^+, \phi_s)$, where $\phi_s = l_{tip}/w$ denotes the solid fraction of the surface.

Drawing inspiration from the work of Rastegari & Akhavan (2019) on the DR scaling in the grooved SHP surfaces in turbulent channel flows, $b^+(w^+, \phi_s)$ is derived from magnitude estimates on the dynamics of turbulence kinetic energy (TKE) within the layer of thickness $\sim w$. Instead of the common primary term $-\langle u_\theta u_r\rangle\, \partial\langle U\rangle/\partial r$ in wall-bounded flows, it is the axial shear term $-\langle u_\theta u_z\rangle\, \partial\langle U\rangle/\partial z$ that dominates the overall production of TKE in the surface layer, which arises from significant axial gradient of azimuthal velocity due to the slip/no-slip patterns of the grooved surface. Rastegari & Akhavan (2019) demonstrate that the additional production of TKE through these axial shear layers is dissipated by the turbulent eddies above the no-slip regions, such that

$$\left\{-\langle u_\theta u_z\rangle \frac{\partial\langle U\rangle}{\partial z}\right\}_{shear\ layer} \sim \left\{\upsilon\langle s_{ij}s_{ij}\rangle\right\}_{no\ slip}. \tag{3.4}$$

On the left-hand side, utilizing the mixing length theory, the Reynolds stress $-\langle u_\theta u_z\rangle$ is estimated as $-\langle u_\theta u_z\rangle \sim u' l\, \partial\langle U\rangle/\partial z$, where the characteristic velocity of the largest eddies u' and their size l are given by the geometric average of the corresponding scale at $r = 0$ and $r \sim w$, specifically $u' \sim \sqrt{u_{\tau n} u_\tau} = \sqrt{u_\tau/\sqrt{\phi_s}\, u_\tau}$ and $l \sim \sqrt{\delta_v\, w}$, while $\partial\langle U\rangle/\partial z$ is estimated as U_{ss}/w, where $U_{ss} = U_s/(1-\phi_s)$ is the average slip velocity of the microstructure walls. On the right-hand side, the fluctuating strain rate above the no-slip regions can be given by characteristic velocity dividing its associated inner length scale, i.e. $s_{ij} \sim u'/\delta'$, where $\delta' = \upsilon/u'$. Using the estimates above, the scaling is given as

$$U_s^+ = b^+ = K\left\{(1-\phi_s)\,\phi_s^{-3/8}\right\}\left\{w^+\right\}^{3/4}, \tag{3.5}$$

where the multiplicative coefficient K is determined to be 0.34 through linear regression. Here, the experimental results of b^+, or equivalently U_s^+ under the Navier slip hypothesis, is given by (3.3) based on torque measurement.

As indicated in (3.5), contributions of geometrical features to wall slip consist of two parts. On the one hand, the decrease in solid fraction ϕ_s will give rise to reduced solid friction and thus enhanced slip. On the other hand, as the dimensionless groove width $\tilde{w}$ increases, the axial gradients of mean velocity and the TKE production in the shear layer decline, which also represents a larger wall slip.

Figure 8(a) presents the experimental results of b^+ varying with $\tilde{w}$ and Re. The wall slip is enhanced with increasing $\tilde{w}$ and Re within the investigated parameter space, aligning with the observed trend of DR depicted in figure 4. Figure 8(b) shows $\{\phi_s^{3/8}/(1-\phi_s)\}b^+$ computed from these experimental databases, which can be seen to scale as $\{w^+\}^{3/4}$ in agreement with (3.5). We also explored the scaling dependence between the shift $\Delta\omega^+$ and w^+ as well as ϕ_s, as shown in figures 9(a) and 9(b), and the multiplicative coefficient is determined to be 0.2 through linear regression.

Accurate prediction of the friction coefficient C_f is essential when dealing with turbulent boundary layers affected by surface roughness. The joint equations (3.3) and (3.5) are

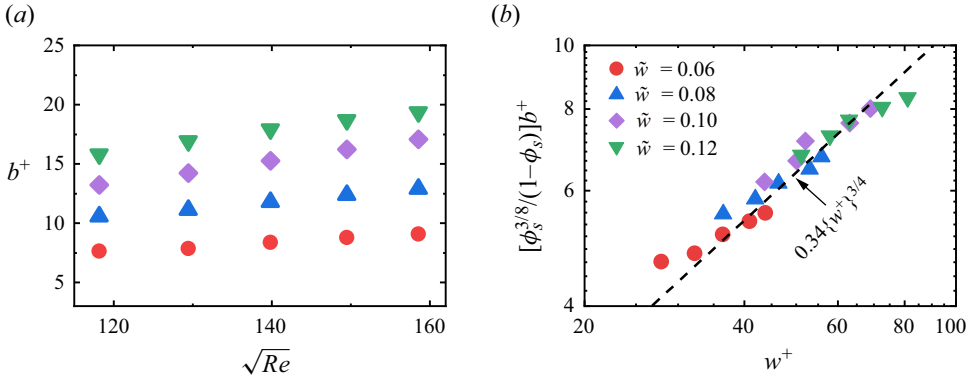

Figure 8. (*a*) Plots of b^+ as a function of Re and $\tilde{w}$, where a solid symbol denotes experimental. (*b*) The logarithmic plot verifying the scaling of b^+, with the dashed lines showing the prediction of (3.5).

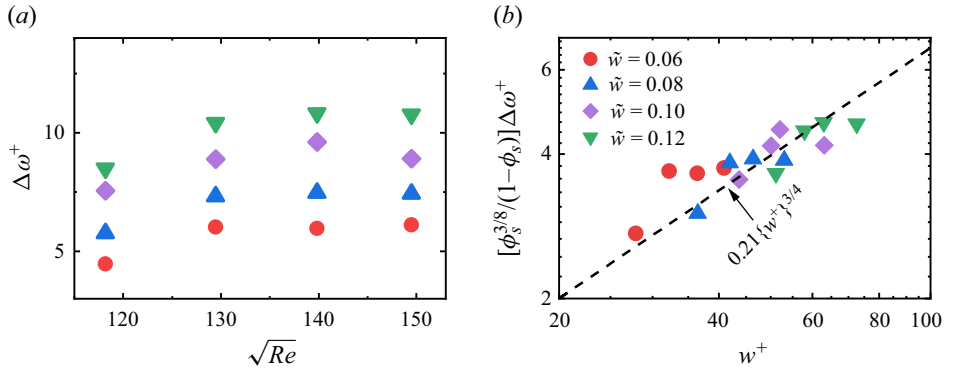

Figure 9. (*a*) Plots of $\Delta\omega^+$ as a function of Re and $\tilde{w}$, where a solid symbol denotes experimental. (*b*) The logarithmic plot verifying the scaling of $\Delta\omega^+$, with the dashed lines showing the prediction of the shift $\Delta\omega^+$.

effective in predicting C_f, i.e.

$$\sqrt{\frac{2}{C_f}} = M \ln\left(Re\sqrt{\frac{C_f}{2}}\right) + N + K\left\{(1-\phi_s)\,\phi_s^{-3/8}\right\}\left\{w^+\right\}^{3/4}. \tag{3.6}$$

Initially, (3.5) is used to determine b^+ from the known values of w^+ and ϕ_s. The calculated b^+ is then substituted into (3.3) to calculate C_f. This method requires only the parameters w, ϕ_s and Re to predict the friction coefficient. As shown in figure 4, comparing the theoretical model with the experimental values shows that both the friction coefficient C_f and DR are predicted with high accuracy. The theoretical model can accurately predict friction and drag behaviour across surface roughness levels and flow conditions. In this way, theoretical models help engineers and researchers to understand complex multiscale interaction between the microstructural parameters (w and ϕ_s) and the flow parameter (Re) on the magnitude of DR, predicting complex flow phenomena that may be encountered in practical applications, providing a scientific basis for design optimization.

In terms of errors, the theory overpredicts b^+ at large w with high Re, and underpredicts it at lower Re. In the former cases, the plastrons over grooves undergo fluctuations and

become challenging to maintain, leading to partial wetting and deterioration of the SHP surfaces, primarily adjacent to the hydrophilic tip of the grooves, as shown in figure 2(*b*). The partial deterioration of the plastron, or in other words, the depinning of the liquid–gas interface, will increase the solid fraction ϕ_s. According to (3.5), as ϕ_s increases, the dimensionless slip of the surface declines, indicating the overestimate of b^+. Nevertheless, at lower *Re*, the underprediction of b^+ can be attributed to the curvature effect of the TC flow, which is more pronounced at finite *Re* where the boundary layer is rather thick and curved (Berghout *et al.* 2020). Specifically, the curvature-induced TKE production ($P_{curvature}$) in the cylindrical coordinate should be taken into account in (3.4) (Berghout *et al.* 2020), i.e.

$$P_{shear\ layer} + P_{curvature} = \varepsilon_{no\text{-}slip}, \tag{3.7}$$

where $P_{curvature} = (1/r)\langle u_\theta u_r\rangle\langle U\rangle = -u'l(\langle U\rangle/r)(\partial\langle U\rangle/\partial r) > 0$. This additional positive term will emerge on the left-hand side of (3.5) at finite *Re* in TC flow, resulting in the overprediction of b^+ if the curvature effect is neglected. However, compared to the results from Van Buren & Smits (2017) where the optimum groove size before surface failure is $w^+ \approx 35$, the counterpart in our experimental set-up can reach $w^+ \approx 75$ or even higher due to the stabilization provided by hydrophilic tips of SHP grooves.

4. Conclusion

In this study, we incorporated hydrophilic tips in SHP grooves to enhance the stability of the plastron while retaining the appreciable drag reduction in TC flow at high *Re*. Here, *DR* with groove width $\tilde{w} = 0.12$ reached 62 % at $Re = 2.79 \times 10^4$. Based on torque and PIV measurements, the underlying mechanism of drag reduction was revealed. The air-filled grooves generated a significant wall slip, leading to a notable decrease in the intensity of Taylor rolls and angular momentum transport, consequently reducing drag. This phenomenon becomes more pronounced with increasing $\tilde{w}$. Moreover, a theoretical model was established based on angular momentum defect theory and magnitude estimate, in order to quantify the multiscale relationship between global response and geometrical and driving parameters. The surface solid fraction ϕ_s and the groove width with respect to inner scales w^+ turn out to be crucial to the friction drag. A decrease in the surface solid fraction can reduce wall shear, and an increase in the groove width can weaken turbulence kinetic energy production, rendering enhanced slip and drag reduction. Our work provides potential implications on the design and optimization of drag-reducing surfaces for enhancing efficiency and performance in various engineering applications, including transportation, marine engineering, and other relevant processes.

Supplementary movie. A supplementary movie is available at https://doi.org/10.1017/jfm.2024.948.

Funding. We are grateful for stimulating discussions with J. Wang and F. Xu, and for the support of the National Natural Science foundation of China (NSFC) under grant nos 12293000, 12293001, 11988102, 12172006, U2141251, 12202010, and Laoshan Laboratory (no. LSKJ202200500).

Declaration of interests. The authors report no conflict of interest.

Author ORCIDs.
Xiaochao Liu https://orcid.org/0000-0001-6146-0658;
Chenxi You https://orcid.org/0009-0006-2458-7493;
Yanlin Cao https://orcid.org/0009-0003-9026-2775;
Baorui Xu https://orcid.org/0000-0002-4345-0496;
Yantao Yang https://orcid.org/0000-0001-5065-2769;

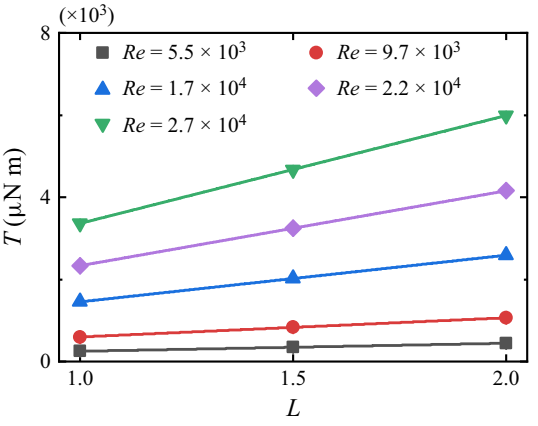

Figure 10. The calibration of the torque measurements. The torque contribution from the von Kármán flow at the ends of the system can be determined as the vertical intercept of the fitting line.

Hongyuan Li https://orcid.org/0000-0003-1048-4670;
Pengyu Lv https://orcid.org/0000-0003-2265-4366;
Chao Sun https://orcid.org/0000-0002-0930-6343;
Huiling Duan https://orcid.org/0000-0003-1478-5649.

Appendix A

In TC flow, the total system torque T_{total} can be decomposed into two parts: (i) the torque T due to the shear stress on the wall of the inner rotor; (ii) the torque T_{end} contributed by the von Kármán flow at the end plates. Considering the linear relationship between T and the height of the inner cylinder (Greidanus *et al.* 2011; Hu *et al.* 2017; Wang *et al.* 2022; Xu *et al.* 2023), T_{end} can be determined from the vertical intercept of the fitting lines. We conducted torque measurement experiments with three different heights (L, $1.5L$, $2L$) of inner rotors, and the results are shown in figure 10. In these calibration experiments, the smooth case was used. The ratio of T_{end} to T_{total} is approximately constant (approximately 22 %) at different Re.

Appendix B

In this study, we provide a supplementary movie comparing the evolution of the liquid–gas interface in V-grooves with and without hydrophilic tips. For $Re = 2.79 \times 10^4$, the liquid–gas interface remains stable in V-grooves with hydrophilic tips, as shown in figure 11(a). In contrast, without hydrophilic tips, buoyancy and pressure cause the air to move upwards, leading to the degradation or disappearance of the air layer, as depicted in figure 11(b).

Appendix C

In this Appendix, we present experimental results of the time-averaged radial velocity $\langle u_r \rangle_t$ in the r–z plane, as shown in figure 12. It is evident that the size of rolls on the grooved surface is larger than that on the smooth surface, and the roll size increases as the groove

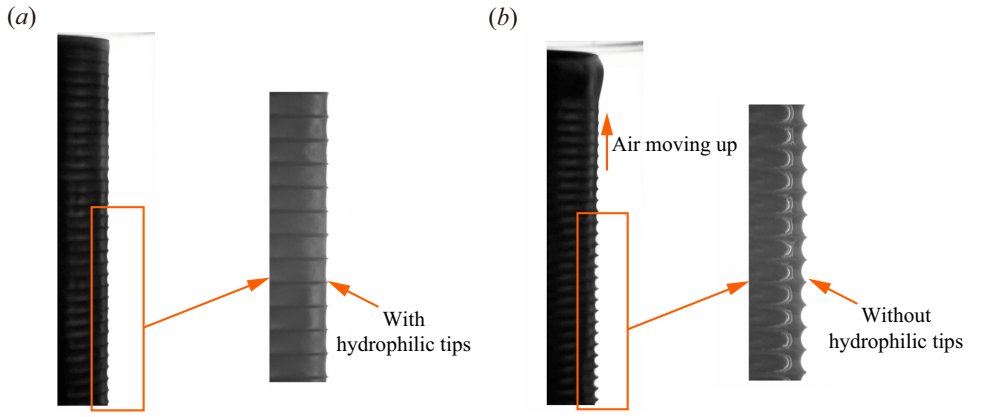

Figure 11. The comparison of the stability of liquid–gas interfaces at the groove tips with and without hydrophilic tips at $Re = 2.79 \times 10^4$: (*a*) with hydrophilic tips; (*b*) without hydrophilic tips.

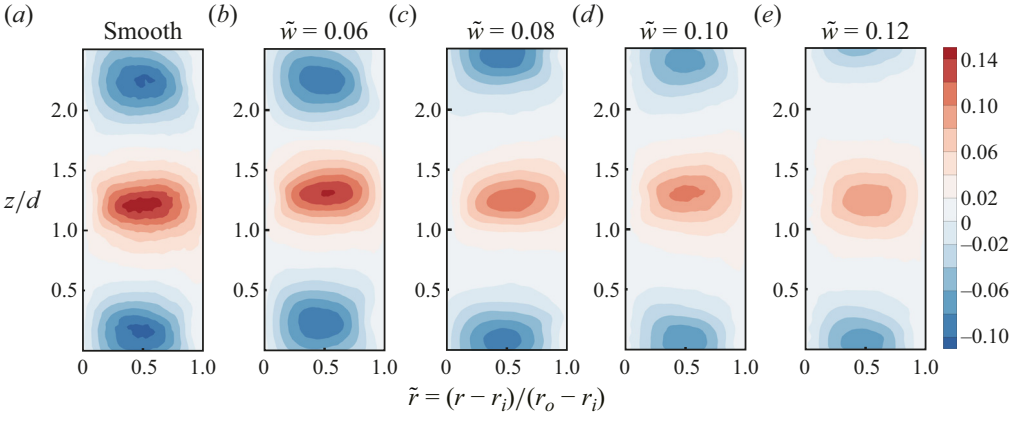

Figure 12. Temporally averaged radial velocity results $\langle u_r \rangle_t$ from experiments at $Re = 1.12 \times 10^4$.

width increases, which is consistent with the findings about the distribution of the Taylor roll in figure 6.

Appendix D

We explore the relationship between C_f and DR as a function of w^+ and ϕ_s. As shown in figure 13, the data of C_f and DR from different Re and $\tilde{w}$ are not fully collapsed, which suggests that the Re effect still exists for C_f and DR. Specifically, the Re effect occurs in the logarithmic term of C_f in (3.3), and in the $C_{f,smooth}$ term of $DR = 1 - C_{f,w}/C_{f,smooth}$. However, since the slip term $b^+ = b/\delta_v = b/(r_o - r_i)\, Re\, \sqrt{C_f/2}$ in (3.3) varies linearly with $Re\, \sqrt{C_f/2}$, faster than the logarithmic term, the Re effect tend to diminish at relatively high Re, resulting in a linear relationship between $\sqrt{2/C_f}$ and b^+, as shown in figure 13(*a*).

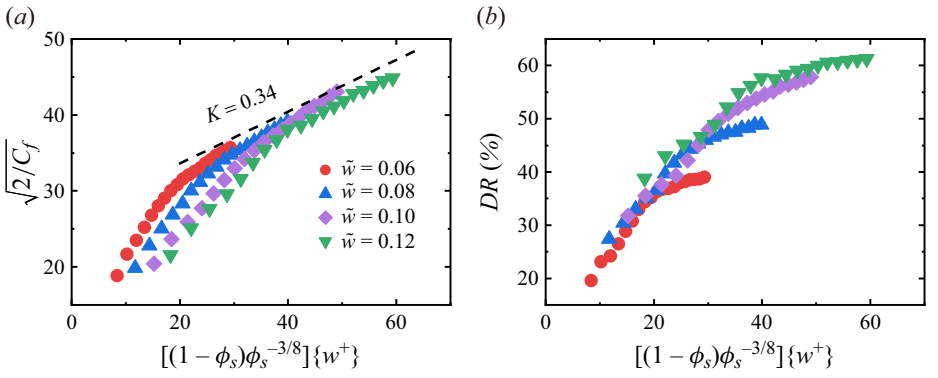

Figure 13. The scaling of C_f and DR with surface microtexture parameters (w^+, ϕ_s) in turbulent TC flow from different Re and $\tilde{w}$, with the dashed line showing the prediction for C_f.

References

Berghout, P., Bullee, P.A., Fuchs, T., Scharnowski, S., Kähler, C.J., Chung, D., Lohse, D. & Huisman, S.G. 2021 Characterizing the turbulent drag properties of rough surfaces with a Taylor–Couette setup. *J. Fluid Mech.* **919**, 1–21.

Berghout, P., Verzicco, R., Stevens, R.J.A.M., Lohse, D. & Chung, D. 2020 Calculation of the mean velocity profile for strongly turbulent Taylor–Couette flow at arbitrary radius ratios. *J. Fluid Mech.* **905**, A11.

Brauckmann, H.J. & Eckhardt, B. 2013 Direct numerical simulations of local and global torque in Taylor–Couette flow up to $Re = 30\,000$. *J. Fluid Mech.* **718**, 398–427.

Cao, Y., Liu, X., Zhang, L., Wu, Y., You, C., Li, H., Duan, H., Huang, J. & Lv, P. 2024 Water impalement resistance and drag reduction of the superhydrophobic surface with hydrophilic strips. *ACS Appl. Mater. Interfaces* **16** (13), 16973–16982.

Daniello, R.J., Waterhouse, N.E. & Rothstein, J.P. 2009 Drag reduction in turbulent flows over superhydrophobic surfaces. *Phys. Fluids* **21** (8), 85–103.

Eckhardt, B., Grossmann, S. & Lohse, D. 2007 Torque scaling in turbulent Taylor–Couette flow between independently rotating cylinders. *J. Fluid Mech.* **581**, 221–250.

Fukagata, K., Kasagi, N. & Koumoutsakos, P. 2006 A theoretical prediction of friction drag reduction in turbulent flow by superhydrophobic surfaces. *Phys. Fluids* **18**, 051703.

Gose, J.W., Golovin, K., Boban, M., Mabry, J.M., Tuteja, A., Perlin, M. & Ceccio, S.L. 2018 Characterization of superhydrophobic surfaces for drag reduction in turbulent flow. *J. Fluid Mech.* **845**, 560–580.

Greidanus, A.J., Delfos, R. & Westerweel, J. 2011 Drag reduction by surface treatment in turbulent Taylor–Couette flow. In *J. Phys. Conf. Ser.*, vol. 318, pp. 1–10. IOP Publishing.

Grossmann, S. & Lohse, D. 2011 Multiple scaling in the ultimate regime of thermal convection. *Phys. Fluids* **23**, 045108.

Grossmann, S., Lohse, D. & Sun, C. 2016 High-Reynolds number Taylor–Couette turbulence. *Annu. Rev. Fluid Mech.* **48** (1), 53–80.

Hu, H., *et al.* 2017 Significant and stable drag reduction with air rings confined by alternated superhydrophobic and hydrophilic strips. *Sci. Adv.* **3** (9), e1603288.

Im, H.J. & Lee, J.H. 2017 Comparison of superhydrophobic drag reduction between turbulent pipe and channel flows. *Phys. Fluids* **29**, 095101.

Jeganathan, V., Alba, K. & Ostilla-Mónico, R. 2021 Controlling secondary flows in Taylor–Couette flow using stress-free boundary conditions. *J. Fluid Mech.* **922**, A17.

Jeganathan, V., Shannak, T., Alba, K. & Ostilla-Mónico, R. 2023 Controlling secondary flows in Taylor–Couette flow using axially spaced superhydrophobic surfaces. *J. Fluid Mech.* **969**, A18.

Jelly, T., Jung, S.Y. & Zaki, T. 2014 Turbulence and skin friction modification in channel flow with streamwise-aligned superhydrophobic surface texture. *Phys. Fluids* **26**, 095102.

Ji, S., Li, H., Du, Z., Lv, P. & Duan, H. 2023 Influence of interfacial coupled flow on slip boundary over a microstructured surface. *Phys. Rev. Fluids* **8**, 054003.

JUNG, T., CHOI, H. & KIM, J. 2016 Effects of the air layer of an idealized superhydrophobic surface on the slip length and skin-friction drag. *J. Fluid Mech.* **790**, R1.

LI, H., JI, S., TAN, X., LI, Z., XIANG, Y., LV, P. & DUAN, H. 2020*a* Effect of Reynolds number on drag reduction in turbulent boundary layer flow over liquid–gas interface. *Phys. Fluids* **32**, 12211.

LI, H., LI, Z., TAN, X., WANG, X., HUANG, S., XIANG, Y., LV, P. & DUAN, H. 2020*b* Three-dimensional backflow at liquid–gas interface induced by surfactant. *J. Fluid Mech.* **899**, A8.

MARTELL, M.B., ROTHSTEIN, J.P. & PEROT, J.B. 2010 An analysis of superhydrophobic turbulent drag reduction mechanisms using direct numerical simulation. *Phys. Fluids* **22**, 065102.

MIN, T. & KIM, J. 2004 Effects of hydrophobic surface on skin-friction drag. *Phys. Fluids* **16** (7), L55–L58.

OSTILLA-MÓNICO, R., VERZICCO, R., GROSSMANN, S. & LOHSE, D. 2016 The near-wall region of highly turbulent Taylor–Couette flow. *J. Fluid Mech.* **788**, 95–117.

PARK, H., CHOI, C. & KIM, C.J. 2021 Superhydrophobic drag reduction in turbulent flows: a critical review. *Exp. Fluids* **62** (2), 1–29.

PARK, H., PARK, H. & KIM, J. 2013 A numerical study of the effects of superhydrophobic surface on skin-friction drag in turbulent channel flow. *Phys. Fluids* **25**, 110815.

PARK, H., SUN, G. & KIM, C.J. 2014 Superhydrophobic turbulent drag reduction as a function of surface grating parameters. *J. Fluid Mech.* **747**, 722–734.

RAJAPPAN, A., GOLOVIN, K., TOBELMANN, B., PILLUTLA, V., ABHIJEET, A., CHOI, W., TUTEJA, A. & MCKINLEY, G.H. 2019 Influence of textural statistics on drag reduction by scalable, randomly rough superhydrophobic surfaces in turbulent flow. *Phys. Fluids* **31**, 042107.

RASTEGARI, A. & AKHAVAN, R. 2015 On the mechanism of turbulent drag reduction with super-hydrophobic surfaces. *J. Fluid Mech.* **773**, R4.

RASTEGARI, A. & AKHAVAN, R. 2018 The common mechanism of turbulent skin-friction drag reduction with superhydrophobic longitudinal microgrooves and riblets. *J. Fluid Mech.* **838**, 68–104.

RASTEGARI, A. & AKHAVAN, R. 2019 On drag reduction scaling and sustainability bounds of superhydrophobic surfaces in high Reynolds number turbulent flows. *J. Fluid Mech.* **864**, 327–347.

ROSENBERG, B.J., VAN BUREN, T., FU, M.K. & SMITS, A.J. 2016 Turbulent drag reduction over air- and liquid-impregnated surfaces. *Phys. Fluids* **28**, 015103.

ROTHSTEIN, J. 2010 Slip on superhydrophobic surfaces. *Annu. Rev. Fluid Mech.* **42**, 89–109.

SRINIVASAN, S., KLEINGARTNER, J.A., GILBERT, J.B, COHEN, R.E., MILNE, A.J. & MCKINLEY, G.H. 2015 Sustainable drag reduction in turbulent Taylor–Couette flows by depositing sprayable superhydrophobic surfaces. *Phys. Rev. Lett.* **114** (1), 014501.

THIELICKE, W. & SONNTAG, R. 2021 Particle image velocimetry for MATLAB: accuracy and enhanced algorithms in PIVlab. *J. Open Res. Softw.* **9** (4).

VAN BUREN, T. & SMITS, A.J. 2017 Substantial drag reduction in turbulent flow using liquid-infused surfaces. *J. Fluid Mech.* **827**, 448–456.

VAN DER VEEN, R.C., HUISMAN, S.G., MERBOLD, S., HARLANDER, U., EGBERS, C., LOHSE, D. & SUN, C. 2016 Taylor–Couette turbulence at radius ratio: scaling, flow structures and plumes. *J. Fluid Mech.* **799**, 334–351.

WANG, C., YI, L., JIANG, L. & SUN, C. 2022 How do the finite-size particles modify the drag in Taylor–Couette turbulent flow. *J. Fluid Mech.* **937**, A15.

XU, B., LI, H., LIU, X., XIANG, Y., LV, P., TAN, X., ZHAO, Y., SUN, C. & DUAN, H. 2023 Effect of micro-grooves on drag reduction in Taylor–Couette flow. *Phys. Fluids* **35**, 043608.

ZHANG, J., TIAN, H., YAO, Z., HAO, P. & JIANG, N. 2015 Mechanisms of drag reduction of superhydrophobic surfaces in a turbulent boundary layer flow. *Exp. Fluids* **56**, 1–13.

ZHU, X., OSTILLA-MÓNICO, R., VERZICCO, R. & LOHSE, D. 2016 Direct numerical simulation of Taylor–Couette flow with grooved walls: torque scaling and flow structure. *J. Fluid Mech.* **794**, 746–774.